Available online at www.sciencedirect.com
ScienceDirect
Journal of Computational Physics 225 (2007) 995–1019
JOURNAL OF COMPUTATIONAL PHYSICS
www.elsevier.com/locate/jcp

Optimised boundary compact finite difference schemes for computational aeroacoustics

Jae Wook Kim *

Aeronautics and Astronautics, School of Engineering Sciences, University of Southampton, Southampton SO17 1BJ, UK

Received 21 January 2006; received in revised form 20 November 2006; accepted 10 January 2007
Available online 20 January 2007

Abstract

A set of optimised boundary closure schemes is presented for use with compact central finite difference schemes in computational aeroacoustics (CAA) involving non-trivial boundaries. The boundary schemes are given in a form of non-central compact finite differences. They maintain fourth-order accuracy, a pentadiagonal matrix system and seven-point stencil which the main interior scheme employs. This paper introduces a new strategy to optimise the boundary schemes in the spectral domain and achieve the best resolution characteristics given a strict tolerance for the dispersion and dissipation errors. The boundary schemes are derived from sophisticated extrapolation of solutions outside the domain. The extrapolation functions are devised by combining polynomials and trigonometric series which contain extra control variables used to optimise the resolution characteristics. The differencing coefficients of the boundary schemes are determined in association with the existing coefficients of the interior scheme which is also optimised through an improved procedure in this paper. The accuracy of the proposed schemes is demonstrated by their application to CAA benchmark problems.

Keywords: Compact schemes; Boundary closure; Optimisation; Computational aeroacoustics

1. Introduction

During the last decade compact finite difference/volume schemes have been used widely in various areas including CAA (computational aeroacoustics), DNS (direct numerical simulation) and LES (large eddy simulation) [1–7]. The compact schemes were developed to perform more precise calculation of spatial flux derivatives involved in the governing equations. They are implicit schemes associated with banded Hermitian (normally tridiagonal or pentadiagonal) matrix systems, which are solved by so-called LU-decomposition

* Tel.: +44 23 8059 4886.
E-mail address: j.w.kim@soton.ac.uk

0021-9991/$ - see front matter
doi:10.1016/j.jcp.2007.01.008

procedures. Recently many efforts have been made to improve their spectral resolution characteristics through Fourier analysis since it was shown by Kim and Lee [8] that increasing the resolution capability rather than the truncation order could enhance the overall accuracy more effectively. As a result several types of compact schemes were successfully optimised so as to show the best resolution characteristics for their own purposes [9–12]. Due to their very low dissipative and dispersive performance the optimised compact schemes have been developed for problems that demand long-time precision so that the high-wavenumber errors in particular can be kept small.

Compact schemes normally use wide differencing stencils of up to seven points. Most of them are based on central differences to minimise dissipation in unsteady computations. They are supposed to be used on interior nodes only and generally they are not feasible near the boundaries unless the exterior solutions are known a priori. Therefore, for a practical application, a set of non-central compact schemes must be designed and used near the boundaries in order to close the Hermitian matrix. There are a few simple boundary schemes being used for this purpose [1,7,10–12]. However, due to the over-biased asymmetric stencils without proper optimisation, they may not reproduce the high level of resolution characteristics that the interior schemes genuinely provide. Accordingly they are prone to significantly high error levels in both dissipative and dispersive ways.

A common practice to suppress the excessive errors from the boundary schemes is to decrease the grid spacing near the boundaries until the level of errors becomes similar to that from the interior schemes. In that circumstance the computational cost increases considerably because the compressed grid spaces require a reduction in the time step size. Such a loss of efficiency is quite detrimental to a CAA task that is firmly based on unsteady calculation. In addition the matter gets worse when the problem involves a wall boundary in viscous flow where the highest precision is required on the boundary. However little progress has been made in making a significant improvement of the boundary schemes to date since Kim and Lee [13] showed the potential for a successful optimisation. Carpenter et al. [14] suggested a few classes of stable boundary compact schemes with eigenvalue analyses, whose actual performances were left unknown.

In this paper a complete set of boundary compact schemes is presented in an extended formalism from the previous works [13,14]. The proposed boundary schemes are designed for use with a fourth-order pentadiagonal interior compact scheme which is based on central differences with a seven-point stencil. They maintain the same fourth-order accuracy with a seven-point stencil, which is especially arranged to complete the pentadiagonal matrix system. The boundary schemes are derived from sophisticated extrapolation of solutions beyond the boundary. The extrapolation functions are devised by linear combinations of polynomials and trigonometric series which contain extra control variables used to optimise the resolution characteristics of the resulting schemes. The differencing coefficients of the boundary schemes are determined in association with the existing coefficients of the interior scheme. The accuracy of the boundary schemes is then demonstrated by their application to CAA benchmark problems.

The organisation of the paper is as follows. Section 2 gives a brief introduction to an optimised interior compact scheme to be used in the present work. Section 3 describes the main idea of developing the boundary closure strategy for compact schemes. Section 4 shows a detailed procedure to optimise the boundary schemes in order to achieve the best resolution characteristics. Section 5 exhibits the results of computation in comparison with analytic solutions and validates the numerical accuracy and performance of the new boundary schemes. Finally concluding remarks are made in Section 6.

2. Optimised interior compact finite difference scheme

In this section the central compact finite difference scheme to be used on interior nodes is briefly introduced before entering the main part. The optimisation procedure to achieve the best resolution characteristics of the scheme is reviewed, and an enhanced optimisation technique is also proposed. The improved resolution characteristics are compared with the previous ones reported in [1,8]. The resulting coefficients are essentially associated with the development of boundary compact schemes to be introduced in the next section.

2.1. Interior compact finite difference scheme

The interior scheme considered in the present work is a pentadiagonal type of central compact finite difference scheme. It is a generalisation of the Hermitian scheme based on a seven-point stencil. It may be expressed as

$$\beta\bar{f}'_{i-2} + \alpha\bar{f}'_{i-1} + \bar{f}'_i + \alpha\bar{f}'_{i+1} + \beta\bar{f}'_{i+2} = \frac{1}{\Delta x}\sum_{m=1}^{3} a_m(f_{i+m} - f_{i-m}), \tag{1}$$

where f_i and f'_i represent an objective function $f(x)$ and its spatial derivative $\partial f(x)/\partial x$, respectively, at a location of interest x_i. The bar "‾" represents the numerical approximation. The spatial interval $\Delta x = x_{i+1} - x_i$ is a constant independent of the index i in the computational domain where all the grid points are equally spaced. Matching the same terms from the Taylor series expansion of Eq. (1) up to fourth-order results in the following two equations:

$$1 + 2(\alpha + \beta) = 2\sum_{m=1}^{3} m a_m, \tag{2}$$

$$3(\alpha + 2^2\beta) = \sum_{m=1}^{3} m^3 a_m. \tag{3}$$

Eq. (1) can also be analysed in the spectral domain through Fourier transformation. The finite difference equation (1) is a special case of the following equation with respect to the continuous variable x:

$$\beta\bar{f}'(x-2\Delta x) + \alpha\bar{f}'(x-\Delta x) + \bar{f}'(x) + \alpha\bar{f}'(x+\Delta x) + \beta\bar{f}'(x+2\Delta x) = \frac{1}{\Delta x}\sum_{m=1}^{3} a_m[f(x+m\Delta x) - f(x-m\Delta x)] \tag{4}$$

which can restore Eq. (1) by setting $x = x_i$. The Fourier transform of the objective function is defined as

$$\tilde{f}(k) = \int_{-\infty}^{\infty} f(x)\mathrm{e}^{-\mathrm{j}kx}\,\mathrm{d}x, \tag{5}$$

where $\mathrm{j} = \sqrt{-1}$, k is the wavenumber and the tilde represents the transformed function. The use of Fourier transform to analyse difference approximations has been discussed and established through a series of literatures as listed in [1]. Taking the Fourier transform of Eq. (4) and through the use of Euler's formula the following equation can be derived:

$$\mathrm{j}\bar{\kappa}\tilde{f}(k)[1 + 2\alpha\cos(\kappa) + 2\beta\cos(2\kappa)] = 2\mathrm{j}\tilde{f}(k)\sum_{m=1}^{3} a_m \sin(m\kappa), \tag{6}$$

where $\kappa \equiv k\Delta x$ is a scaled wavenumber and $\bar{\kappa} \equiv \bar{k}\Delta x$ is a scaled pseudo-wavenumber which implies a certain deviation from the true wavenumber due to the numerical approximation, i.e. $\tilde{f}' = \mathrm{j}k\tilde{f}$ and $\tilde{\bar{f}}' = \mathrm{j}\bar{k}\tilde{f}$ from Eq. (5). Practically $\bar{\kappa}$ should coincide with κ up to as high a value as possible in order to achieve high resolution characteristics. This aim can be pursued by the following procedure.

2.2. Optimisation of interior scheme

It is ideally desirable to make $\bar{\kappa}$ equal to κ in Eq. (6). However it is impossible to build up a perfect match between $\bar{\kappa}$ and κ over the entire range due to the limitations of numerical approximation. Replacing $\bar{\kappa}$ by κ inevitably leads to a certain discrepancy between the left- and the right-hand side of Eq. (6). The discrepancy increases drastically as κ approaches π. This discrepancy actually shows up as a dispersion error of the scheme. Minimising the error over a certain wavenumber range ($0 \leqslant \kappa < \pi$) can lead to maximising the resolution characteristics of the scheme. It turns out that replacing $\bar{\kappa}$ by $(1+\delta)\kappa$ where δ is a constant rather than by

κ in Eq. (6) can be very effective if δ is adjusted properly. Then a total sum of the integrated error based on the l^2-norm over $0 \leqslant \kappa \leqslant r$ can be defined as

$$E = \int_0^r \left\{ (1+\delta)\kappa[1 + 2\alpha\cos(\kappa) + 2\beta\cos(2\kappa)] - 2\sum_{m=1}^{3} a_m \sin(m\kappa) \right\}^2 \left(\frac{\kappa}{r}\right)^n \mathrm{d}\kappa, \tag{7}$$

where $r(< \pi)$ is a factor to determine the integration range and $(\kappa/r)^n$ is a weighting function concentrating on the high wavenumbers.

The conditions for the integrated error to be a local minimum are given by $\partial E/\partial\zeta = 0$ where ζ represents the differencing coefficients α, β or a_m $(m = 1, \ldots, 3)$. The five differencing coefficients remain unknown until five equations are organised and solved for them. Two equations are already available in Eqs. (2) and (3), from the requirement on the order of truncation. The other three come from the minimisation of the integrated error, which are selected as

$$\frac{\partial E}{\partial \alpha} = 0, \quad \frac{\partial E}{\partial \beta} = 0, \quad \frac{\partial E}{\partial a_3} = 0. \tag{8}$$

The coefficients α, β and a_3 are chosen for the minimisation of the integrated error. Although a variety of different combinations of the coefficients can be considered in Eq. (8) – to be discussed in Section 2.3, the author's original choice (α, β, a_3) is based on the fact that they are the extra coefficients disappearing in the standard fourth-order central difference scheme. In summary, by solving the system of linear algebraic Eqs. (2), (3) and (8), all the five coefficients are determined so that the maximum resolution characteristics can be achieved amongst the fourth-order schemes. Practically this demands some trial and error in order to find the best combination of the adjustable constants r, δ and n.

2.3. Resolution characteristics of interior scheme

Once the differencing coefficients are determined then the resolution characteristics must be assessed. The resolution characteristics can be investigated by plotting a profile of the pseudo-wavenumber which is given as a non-linear function of κ from Eq. (6):

$$\bar{\kappa}(\kappa) = \frac{2\sum_{m=1}^{3} a_m \sin(m\kappa)}{1 + 2\alpha\cos(\kappa) + 2\beta\cos(2\kappa)}. \tag{9}$$

This equation dictates that $\bar{\kappa}$ falls to zero when $\kappa = \pi$ regardless of the coefficients, which implies an ultimate limitation on the finite difference based approaches. In order to measure the deviation of $\bar{\kappa}$ from κ in a standardised fashion the relative resolution error is defined as

$$\varepsilon(\kappa) = \left| \frac{\bar{\kappa}(\kappa) - \kappa}{\kappa} \right| \tag{10}$$

which was introduced in [1], where $\varepsilon(\pi) = 1$. Then the resolution performance of the scheme can be investigated by the following quantity:

$$\kappa_c^\sigma = \min(\kappa | \varepsilon(\kappa) = \sigma, 0 < \kappa < \pi) \tag{11}$$

which gives a critical wavenumber up to which the resolution error is within a tolerance limit specified by σ $(\varepsilon(\kappa) \leqslant \sigma$ for $0 \leqslant \kappa \leqslant \kappa_c^\sigma)$. The typical error tolerance is $\sigma = 0.001$ (0.1%) for a sufficient precision level required in CAA (computational aeroacoustics).

Table 1
Coefficients of optimised central compact finite difference schemes

α	β	a_1	a_2	a_3
0.5862704032801503	0.09549533555017055	0.6431406736919156	0.2586011023495066	0.007140953479797375

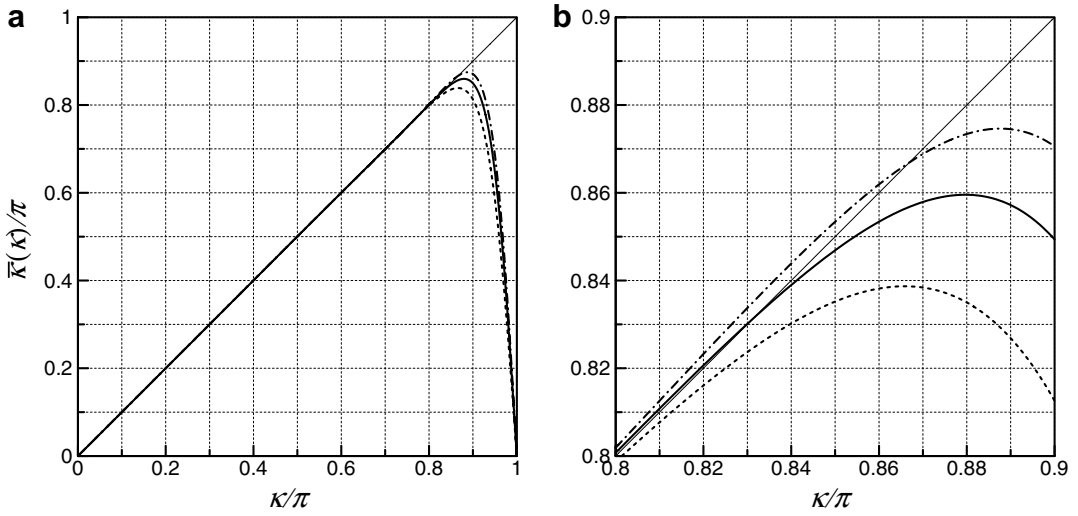

Fig. 1. Pseudo-wavenumber diagrams of fourth-order pentadiagonal central compact schemes on seven-point stencil: (a) entire and (b) enlarged view ($0.8\pi \leqslant \kappa \leqslant 0.9\pi$). (—) exact, (- - -) Lele's [1], (–·–) Kim and Lee's [8], and (—) the present scheme.

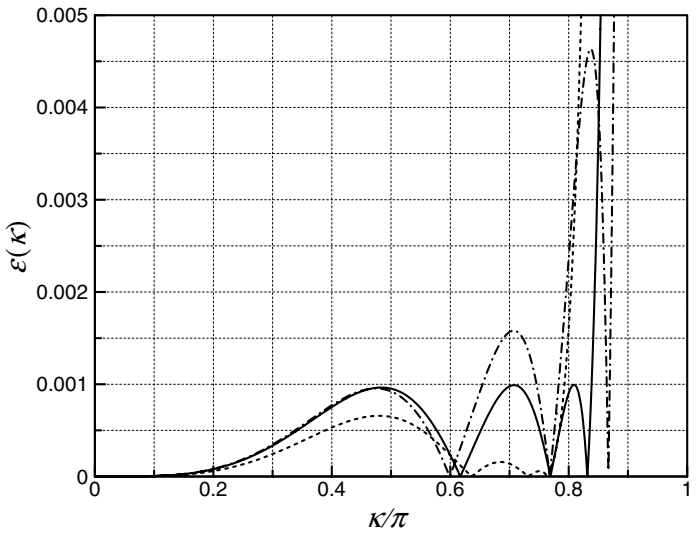

Fig. 2. Resolution error diagrams of fourth-order pentadiagonal central compact schemes on seven-point stencil. (—) exact, (- - -) Lele's [1], (–·–) Kim and Lee's [8], and (—) the present scheme.

In this paper the differencing coefficients of the interior scheme are newly optimised to achieve better resolution characteristics than the previous schemes. In the present work the two adjustable constants r and δ in Eq. (7) are determined to be $r = 2.672$ and $\delta = -0.000233$ through iterative calculations carried out using Mathematica. The optimised coefficients are presented in Table 1. Profiles of the resulting pseudo-wavenumber $\bar{\kappa}(\kappa)$ and the relative resolution error $\varepsilon(\kappa)$ are plotted in Figs. 1 and 2, respectively, compared with those of the previous schemes.

Table 2
Case study on different choices of coefficients in Eq. (8)

	Case 1: (α, β, a_1)	Case 2: (α, β, a_2)	Case 3: (β, a_2, a_3)	Original: (α, β, a_3)
$\kappa_c^{0.1\%}$	0.836π	0.838π	0.838π	$0.839\ \pi$
r	2.661	2.671	2.669	2.672
δ	−0.000210	−0.000246	−0.000260	−0.000233
n	15	11	10	10
α	0.5856396845642288	0.5859572811123209	0.5864696980962217	0.5862704032801503
β	0.09505833117193530	0.09527180900906593	0.09564623994911990	0.09549533555017055
a_1	0.6437151795729501	0.6434288190645918	0.6429512471438849	0.6431406736919156
a_2	0.2578941677285964	0.2582497707129994	0.2588269491578893	0.2586011023495066
a_3	0.007064833568673624	0.007100243210265430	0.007170264195226098	0.007140953479797375

The present scheme has a resolution limit of $\kappa_c^{0.1\%} = 0.839\pi$ which is higher than $\kappa_c^{0.1\%} = 0.791\pi$ from Lele's scheme [1]. Kim and Lee's scheme [8] was obtained using a five times more generous tolerance $\sigma = 0.5\%$ ($\kappa_c^{0.5\%} = 0.876\pi$), which may not be sufficient for the current level of sophistication of CAA calculations. It can be seen in Fig. 2 that Lele's scheme is under-relaxed with vanishing lobes on $0.63\pi \leqslant \kappa \leqslant 0.77\pi$ and sudden burst afterwards. On the other hand Kim and Lee's scheme is over-relaxed with erupting lobes on $0.6\pi \leqslant \kappa \leqslant 0.87\pi$ due to the generous error tolerance (0.5%). It is shown that the present scheme is best optimised to keep a constant amplitude of lobes and reach the maximum resolution range within the strict error tolerance (0.1%).

As briefly mentioned in Section 2.2, different combinations of the coefficients other than the original choice: (α, β, a_3) in Eq. (8) may be selected for the error minimisation. The author has examined the following three different cases: $(\alpha, \beta, a_1), (\alpha, \beta, a_2)$ and (β, a_2, a_3). The results are listed in Table 2 in comparison with the original case. Table 2 shows that all of the three extra combinations achieve as high resolutions as the original one by readjusting the constants r, δ and n as appropriate. One can check that the pseudo-wavenumber profiles collapse nearly on the same curve as well. This investigation evidences that Eq. (7) gives consistent results insensitive to different choices of coefficients in Eq. (8).

3. Boundary closure strategy for compact scheme

This section presents a boundary closure strategy for the optimised interior compact scheme introduced in the previous section. A particular spline function is devised to extrapolate the profiles of the objective function and its first derivative beyond the boundaries virtually. It is shown that the extrapolation functions eventually lead to a set of non-central compact schemes near and at the boundaries. The boundary schemes can be optimised in the spectral domain by virtue of control variables fitted in the extrapolation functions. The detailed procedure follows.

3.1. Extrapolation beyond boundaries

It is obvious that Eq. (1) applies directly on the interior nodes in a range of $3 \leqslant i \leqslant N-3$ where $i = 0$ and N represents boundaries. To be able to keep applying it at the nodes $i = 0, 1$ and 2 (at $i = N-2, N-1$ and N as well) an extrapolation may be used to approximate the objective function profile and its first derivative beyond the boundaries. The following is a spline function from a point of interest (x_i, f_i) near a boundary and its first derivative that may be used for the extrapolation:

$$g_i(x^*) = f_i + \sum_{m=1}^{N_A} p_m (x^*)^m + \sum_{m=1}^{N_B} [q_m \cos(\phi_m x^*) + r_m \sin(\phi_m x^*)], \tag{12}$$

$$g_i'(x^*) = \frac{\mathrm{d}g_i(x^*)}{\mathrm{d}x} = \frac{1}{\Delta x}\left\{ \sum_{m=1}^{N_A} m p_m (x^*)^{m-1} - \sum_{m=1}^{N_B} \phi_m [q_m \sin(\phi_m x^*) - r_m \cos(\phi_m x^*)] \right\}, \tag{13}$$

where $x^* = (x - x_i)/\Delta x$ is the non-dimensional coordinate from the point of interest. The extrapolation function is a linear combination of polynomials and trigonometric series. The constants N_A and N_B represent the orders of each series. The coefficients p_m $(m = 1, \ldots, N_A)$, q_m and r_m $(m = 1, \ldots, N_B)$ should be determined to describe the interior profile of the original function correctly, which allows proper extrapolation to the unknown exterior profile. The control variables ϕ_m $(m = 1, \ldots, N_B)$ are used to optimise the resulting schemes for the best resolution characteristics in Section 4.

A set of extended boundary closure schemes can be derived from combining the extrapolation function with Eq. (1). Imposing $i = 0, 1$ and 2 in Eq. (1) and replacing the exterior terms with the extrapolation functions yields the following equations:

$$i = 0: \quad \beta g_0'(-2) + \alpha g_0'(-1) + \bar{f}_0' + \alpha \bar{f}_1' + \beta \bar{f}_2' = \frac{1}{\Delta x} \sum_{m=1}^{3} a_m [f_m - g_0(-m)], \tag{14}$$

$$i = 1: \quad \beta g_1'(-2) + \alpha \bar{f}_0' + \bar{f}_1' + \alpha \bar{f}_2' + \beta \bar{f}_3' = \frac{1}{\Delta x} \left\{ a_1 (f_2 - f_0) + \sum_{m=2}^{3} a_m [f_{1+m} - g_1(-m)] \right\}, \tag{15}$$

$$i = 2: \quad \beta \bar{f}_0' + \alpha \bar{f}_1' + \bar{f}_2' + \alpha \bar{f}_3' + \beta \bar{f}_4' = \frac{1}{\Delta x} \left\{ \sum_{m=1}^{2} a_m (f_{2+m} - f_{2-m}) + a_3 [f_5 - g_2(-3)] \right\}. \tag{16}$$

It can be seen that three different extrapolation functions $g_0(x^*), g_1(x^*)$ and $g_2(x^*)$ should be determined to make the most of Eqs. (14)–(16). In practice they are determined by matching with some of the existing terms at the interior nodes within a certain range from the boundary. Then they are all expressed by the interior terms. Accordingly Eqs. (14)–(16) change their form and eventually appear as non-central compact schemes. Details on determining the complete set of extrapolation functions follow.

3.2. Determination of extrapolation functions

The present approach seeks to keep the seven-point stencil for the boundary schemes as well as the interior scheme. Therefore the fundamental matching conditions should be

$$\left.\begin{array}{l} g_0(m) \\ g_1(m-1) \\ g_2(m-2) \end{array}\right\} = f_m \quad \text{for } m = 0, \ldots, 6 \tag{17}$$

which delivers seven constraints commonly for the three different extrapolation functions. In addition the first derivatives should also be matched. Taking the interior derivatives left available on the left-hand sides in Eqs. (14)–(16) into account, the additional matching conditions can be arranged as

$$\left.\begin{array}{l} g_0'(m) \\ g_1'(m-1) \\ g_2'(m-2) \end{array}\right\} = \bar{f}_m' \quad \text{for} \begin{cases} m = 0, 1, 2, \\ m = 0, 1, 2, 3, \\ m = 0, 1, 2, 3, 4, \end{cases} \tag{18}$$

which gives three, four and five more constraints according to the model equations. Eqs. (17) and (18) in all provide 10, 11 and 12 constraints for Eqs. (14)–(16), respectively.

The present approach also allows keeping fourth-order truncation accuracy for the boundary schemes as well as the interior scheme, which means $N_A = 4$. The total number of coefficients to be found in Eqs. (12) and (13) is $N_A + 2N_B$, which must be an even number. However the second case in Eq. (18) provides an odd number of constraints. Therefore an extra constraint is required in the case of $i = 1$ to equalise the unknowns and the constraints. Accordingly the following should be satisfied:

$$N_A + 2N_B = \begin{cases} 10 & (i = 0), \\ 11 + 1 \text{ (extra)} & (i = 1), \\ 12 & (i = 2), \end{cases} \tag{19}$$

where the extra constraint for $i = 1$ is given as

$$q_{N_B} = r_{N_B} \tag{20}$$

which indicates that the last two coefficients of the trigonometric series are set to be identical. This may be the simplest way to create an extra constraint without risk considering that the last term affects the least to the series. Taking these conditions into account the combinations of the constants can be arranged as follows:

$$(N_A, N_B) = \begin{cases} (4,3) & (i=0), \\ (4,4) & (i=1), \\ (4,4) & (i=2). \end{cases} \tag{21}$$

Eqs. (17) and (18) can be solved for the coefficients $p_1, \ldots, p_{N_A}, q_1, \ldots, q_{N_B}, r_1, \ldots, r_{N_B}$, then they are expressed by the interior terms $f_0, \ldots, f_6, \bar{f}'_0, \ldots, \bar{f}'_n$ (where $n = 2,\ 3$ and 4 for the cases of $i = 0, 1$ and 2, respectively) depending on the point of interest. However they still involve the unknown variables $\phi_1, \ldots, \phi_{N_B}$ which are used to optimise the resolution characteristics afterwards.

3.3. Derivation of boundary compact schemes

Once all the coefficients of the extrapolation functions are determined the exterior terms are properly extrapolated. The exterior terms can be replaced by some linear combinations of the interior terms, which may turn Eqs. (14)–(16) into the following form:

$$\sum_{m=0}^{M} c_m \bar{f}'_m = \frac{1}{\Delta x} \sum_{m=0}^{6} d_m f_m \tag{22}$$

where $M = 2, 3$ and 4 for the cases of $i = 0, 1$ and 2, respectively, due to the constraints from Eq. (18). The intermediary coefficients c_m $(m = 0, \ldots, M)$ and d_m $(m = 0, \ldots, 6)$ are in practice non-linear functions of ϕ_m $(m = 1, \ldots, N_B)$. Dividing Eq. (22) with c_n ($n = 0, 1$ and 2 for the cases of $i = 0, 1$ and 2, respectively) for normalisation and rearranging the right-hand-side terms ultimately results in the following equations:

$$i = 0: \quad \bar{f}'_0 + \gamma_{01}\bar{f}'_1 + \gamma_{02}\bar{f}'_2 = \frac{1}{\Delta x} \sum_{m=0,\neq 0}^{6} b_{0m}(f_m - f_0), \tag{23}$$

$$i = 1: \quad \gamma_{10}\bar{f}'_0 + \bar{f}'_1 + \gamma_{12}\bar{f}'_2 + \gamma_{13}\bar{f}'_3 = \frac{1}{\Delta x} \sum_{m=0,\neq 1}^{6} b_{1m}(f_m - f_1), \tag{24}$$

$$i = 2: \quad \gamma_{20}\bar{f}'_0 + \gamma_{21}\bar{f}'_1 + \bar{f}'_2 + \gamma_{23}\bar{f}'_3 + \gamma_{24}\bar{f}'_4 = \frac{1}{\Delta x} \sum_{m=0,\neq 2}^{6} b_{2m}(f_m - f_2), \tag{25}$$

which provides the set of non-central boundary compact schemes being sought. These formulations can close the pentadiagonal matrix system at the boundaries and maintain fourth-order of formal accuracy as well as the seven-point stencils throughout. All the coefficients remaining as non-linear functions of ϕ_{m} $(m = 1, \ldots, N_B)$ are finally determined when the optimal control variables are found in Section 4.

4. Optimisation of boundary compact finite difference schemes

This section presents an optimisation procedure for the boundary compact finite difference schemes formulated in the previous section. The pseudo-wavenumbers of the boundary schemes are derived and the unknown control variables are determined to maximise the range of coincidence between the pseudo-wavenumbers and the true wavenumbers. It is shown that the optimised boundary schemes offer significantly improved resolution characteristics compared with the previous ones.

4.1. Fourier analysis of boundary schemes

The Fourier transform of Eqs. (23)–(25) through the same procedure as used in Section 2.1 may be expressed in a simple form as

$$\mathrm{j}\bar{\kappa}\tilde{f}(k)[A(\kappa)+\mathrm{j}B(\kappa)] = \tilde{f}(k)[C(\kappa)+\mathrm{j}D(\kappa)], \tag{26}$$

where the intermediary functions $A(\kappa), B(\kappa), C(\kappa)$ and $D(\kappa)$ are given for each scheme as follows:

$$i=0: \quad \begin{cases} A(\kappa) = 1+\gamma_{01}\cos(\kappa)+\gamma_{02}\cos(2\kappa), \\ B(\kappa) = \gamma_{01}\sin(\kappa)+\gamma_{02}\sin(2\kappa), \\ C(\kappa) = \sum\limits_{m=0,\neq 0}^{6} b_{0m}[\cos(m\kappa)-1], \\ D(\kappa) = \sum\limits_{m=0,\neq 0}^{6} b_{0m}\sin(m\kappa), \end{cases} \tag{27}$$

$$i=1: \quad \begin{cases} A(\kappa) = 1+(\gamma_{10}+\gamma_{12})\cos(\kappa)+\gamma_{13}\cos(2\kappa), \\ B(\kappa) = (\gamma_{12}-\gamma_{10})\sin(\kappa)+\gamma_{13}\sin(2\kappa), \\ C(\kappa) = \sum\limits_{m=0,\neq 1}^{6} b_{1m}\{\cos[(m-1)\kappa]-1\}, \\ D(\kappa) = \sum\limits_{m=0,\neq 1}^{6} b_{1m}\sin[(m-1)\kappa], \end{cases} \tag{28}$$

$$i=2: \quad \begin{cases} A(\kappa) = 1+(\gamma_{21}+\gamma_{23})\cos(\kappa)+(\gamma_{20}+\gamma_{24})\cos(2\kappa), \\ B(\kappa) = (\gamma_{23}-\gamma_{21})\sin(\kappa)+(\gamma_{24}-\gamma_{20})\sin(2\kappa), \\ C(\kappa) = \sum\limits_{m=0,\neq 2}^{6} b_{2m}\{\cos[(m-2)\kappa]-1\}, \\ D(\kappa) = \sum\limits_{m=0,\neq 2}^{6} b_{2m}\sin[(m-2)\kappa]. \end{cases} \tag{29}$$

Accordingly the pseudo-wavenumbers of the boundary schemes are derived from Eq. (26) and they can be represented as

$$\bar{\kappa}(\kappa) = \frac{A(\kappa)D(\kappa)-B(\kappa)C(\kappa)}{A^2(\kappa)+B^2(\kappa)} - \mathrm{j}\frac{A(\kappa)C(\kappa)+B(\kappa)D(\kappa)}{A^2(\kappa)+B^2(\kappa)}, \tag{30}$$

which is a complex function.

The pseudo-wavenumbers can be divided into real ($\mathrm{Re}[\bar{\kappa}(\kappa)]$) and imaginary ($\mathrm{Im}[\bar{\kappa}(\kappa)]$) parts while those of the interior central schemes consist of the real part only. (Note that $Re(z)=a$ and $\mathrm{Im}(z)=b$ are always real numbers where $z=a+\mathrm{j}b$.) Hence the optimisation of the boundary schemes involves an additional task for the imaginary part. The optimisation should be done such that: the real and imaginary part of $\bar{\kappa}(\kappa)$ follow the true wavenumber ($\mathrm{Re}[\bar{\kappa}(\kappa)] \to \kappa$) and zero ($\mathrm{Im}[\bar{\kappa}(\kappa)] \to 0$), respectively, in as wide range of wavenumbers ($0 \leqslant \kappa < \pi$) as possible. Deviations will result in numerical errors where the real part represents dispersive error and the imaginary part represents dissipative error. Those errors should be minimised in order to make the finite difference schemes a good approximation of partial differentiation.

4.2. Optimisation of boundary schemes

As indicated in Section 3.3 the coefficients in Eqs. (22)–(24) still remain as non-linear functions of ϕ_m ($m=1,\ldots,N_B$), the set of control variables consisting in the trigonometric series of Eqs. (12) and (13). The control variables need to be determined so that both dispersive and dissipative numerical errors are minimised. The following quantities are used to measure the errors of the boundary schemes:

$$\varepsilon_R(\kappa) = \left|\frac{\mathrm{Re}[\bar{\kappa}(\kappa)] - \kappa}{\kappa}\right|, \tag{31}$$

$$\varepsilon_I(\kappa) = \left|\frac{\mathrm{Im}[\bar{\kappa}(\kappa)]}{\kappa}\right|, \tag{32}$$

which describe the real and the imaginary part of relative deviation of the pseudo-wavenumber from the true wavenumber. Then the resolution performance of the boundary schemes can be investigated by the following quantities:

$$\kappa_c^\sigma = \frac{1}{2}(\kappa_{Rc}^\sigma + \kappa_{Ic}^\sigma), \tag{33}$$

where

$$\kappa_{Rc}^\sigma = \min(\kappa|\varepsilon_R(\kappa) = \sigma, 0 < \kappa < \pi), \tag{34}$$

$$\kappa_{Ic}^\sigma = \min(\kappa|\varepsilon_I(\kappa) = \sigma, 0 < \kappa < \pi), \tag{35}$$

which gives a critical wavenumber up to which the resolution error is within a tolerance limit specified by σ ($\varepsilon_R(\kappa) \leqslant \sigma$ for $0 \leqslant \kappa \leqslant \kappa_{Rc}^\sigma$ and $\varepsilon_I(\kappa) \leqslant \sigma$ for $0 \leqslant \kappa \leqslant \kappa_{Ic}^\sigma$). It can be noted that the same factor is given to κ_{Rc}^σ and κ_{Ic}^σ in Eq. (33). The factors may be changed in the form of $\kappa_c^\sigma = s\kappa_{Rc}^\sigma + (1-s)\kappa_{Ic}^\sigma$ in order to put more weight on one of them. However the present work keeps $s = 1/2$ without biased weight.

The error tolerance $\sigma = 0.001$ (0.1%) is applied to the boundary scheme for $i = 2$ given by Eq. (25). In the meantime, the error tolerances are relaxed to $\sigma = 0.002$ (0.2%) for $i = 1$ and $\sigma = 0.003$ (0.3%) for $i = 0$, in order to achieve as wide a resolution range of the interior scheme as possible. However the present error tolerances are still smaller than those of the previous schemes [1,11–13]. For instance Kim and Lee's work [13] was done with $\sigma = 0.005$ (0.5%) throughout.

The control variables ϕ_m ($m = 1, \ldots, N_B$) are adjusted to maximise the value of κ_c^σ for each boundary scheme. A set of roots can be found by the Newton–Raphson type of iterative method using the Mathematica. The iteration starts from an initial guess of $\phi_m = m\pi/N_B$ ($m = 1, \ldots, N_B$) and continues until the optimal combination is reached. The final values of ϕ_m and the resolution limits κ_{Rc}^σ, κ_{Ic}^σ and κ_c^σ are listed in Tables 3 and 4 for each boundary scheme. As a result all the coefficients for the optimised boundary schemes are finally determined as presented in Table 5. Profiles of the resulting pseudo-wavenumbers $\mathrm{Re}[\bar{\kappa}(\kappa)]$ and $\mathrm{Im}[\bar{\kappa}(\kappa)]$ as well as the relative resolution errors $\varepsilon_R(\kappa)$ and $\varepsilon_I(\kappa)$ are plotted in Figs. 3–5 in comparison with those of the previous schemes [1,11,13].

Table 3
Optimal values of control variables for boundary compact schemes

Scheme	ϕ_1	ϕ_2	ϕ_3	ϕ_4
$i = 0$	0.147π	0.498π	1.234π	–
$i = 1$	0.190π	0.645π	0.765π	1.260π
$i = 2$	0.140π	0.352π	0.713π	0.788π

Table 4
Resolution limits of optimised boundary compact schemes

Scheme	σ (%)	κ_{Rc}^σ	κ_{Ic}^σ	κ_c^σ
$i = 0$	0.3	0.827π	0.505π	0.666π
$i = 1$	0.2	0.779π	0.780π	0.780π
$i = 2$	0.1	0.911π	0.796π	0.854π

Table 5
Coefficients of optimised boundary compact schemes

Coefficients	$i = 0$	$i = 1$	$i = 2$
γ_{i0}	–	0.08360703307833438	0.03250008295108466
γ_{i1}	5.912678614078549	–	0.3998040493524358
γ_{i2}	3.775623951744012	2.058102869495757	–
γ_{i3}	–	0.9704052014790193	0.7719261277615860
γ_{i4}	–	–	0.1626635931256900
b_{i0}	–	−0.3177447290722621	−0.1219006056449124
b_{i1}	−3.456878182643609	–	−0.6301651351188667
b_{i2}	5.839043358834730	−0.02807631929593225	–
b_{i3}	1.015886726041007	1.593461635747659	0.6521195063966084
b_{i4}	−0.2246526470654333	0.2533027046976367	0.3938843551210350
b_{i5}	0.08564940889936562	−0.03619652460174756	0.01904944407973912
b_{i6}	−0.01836710059356763	0.004080281419108407	−0.001027260523947668

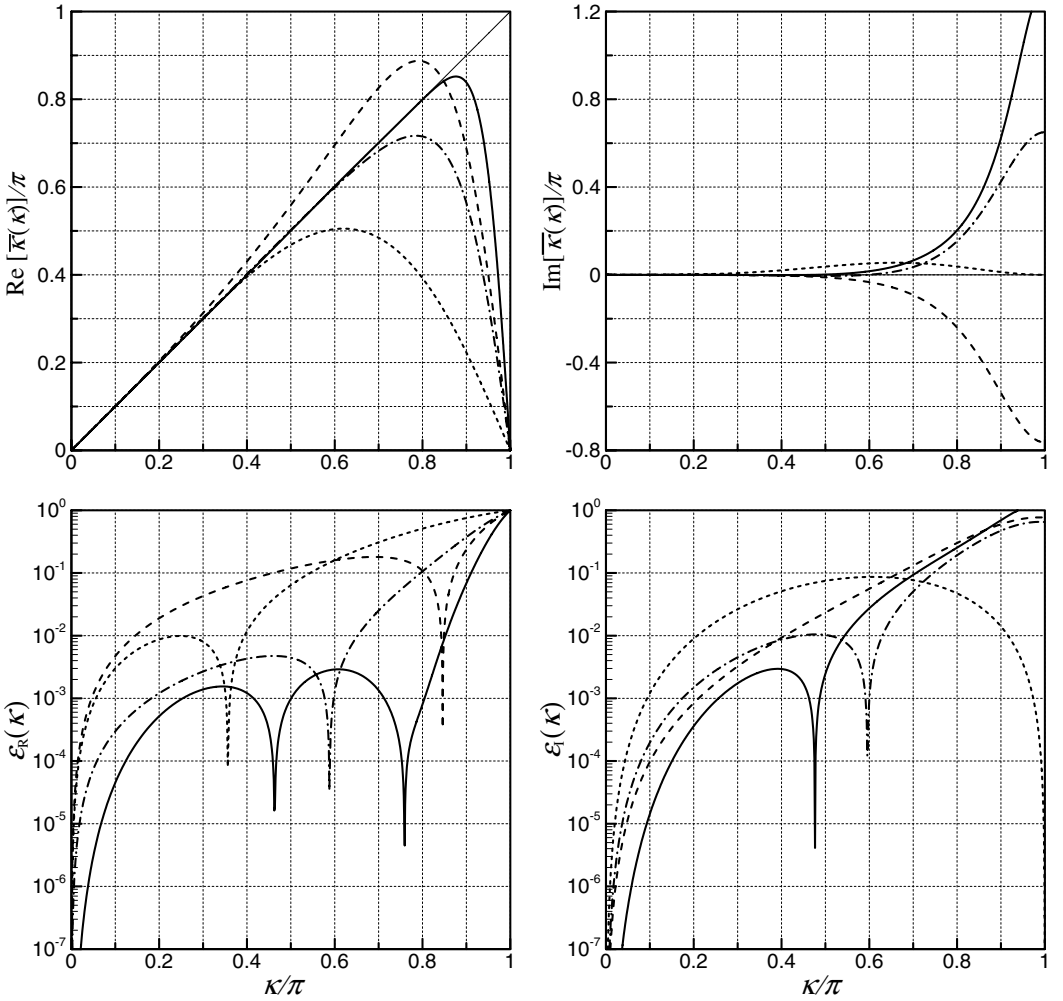

Fig. 3. Pseudo-wavenumber and resolution error diagrams of boundary compact schemes for $i = 0$. (—) exact, (- - -) Lele's [1], (– – –) Lee and Seo's [11], (–·–) Kim and Lee's [13], and (—) the present scheme.

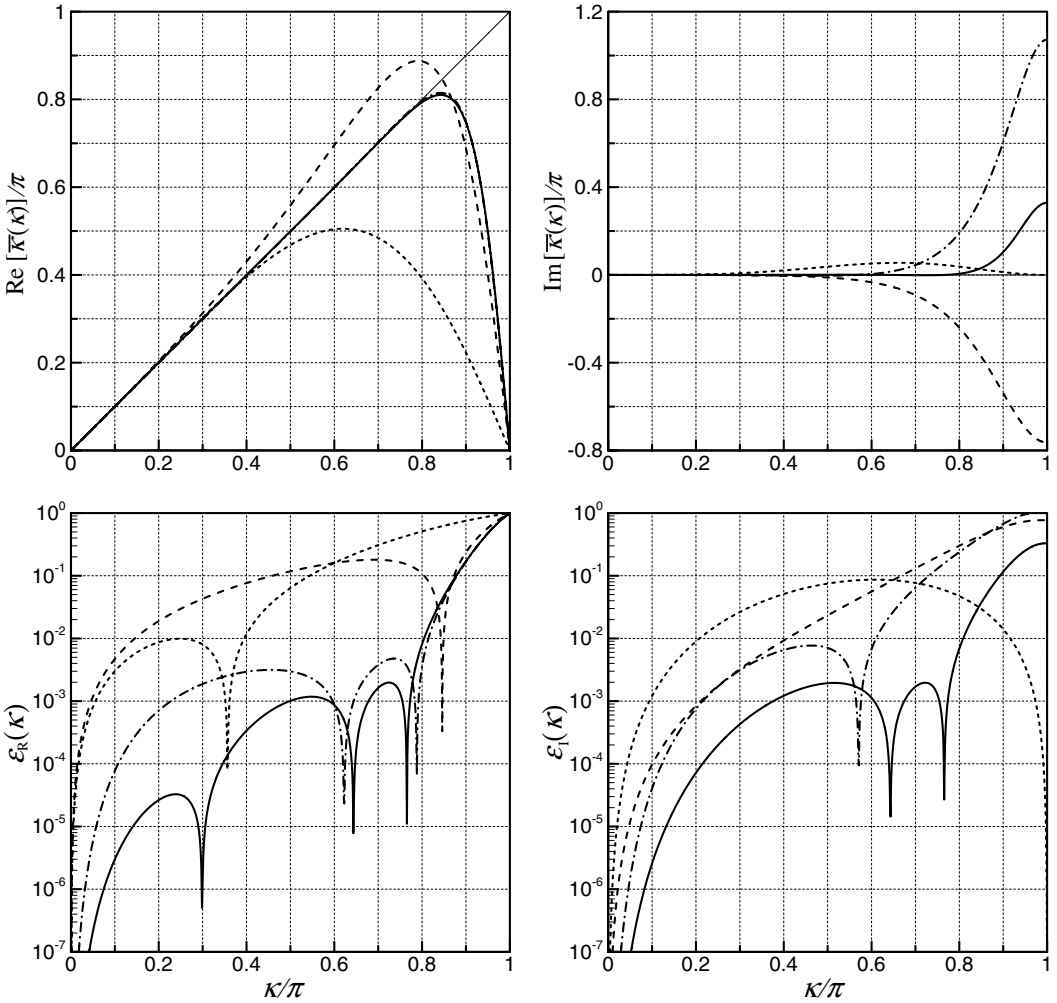

Fig. 4. Pseudo-wavenumber and resolution error diagrams of boundary compact schemes for $i = 1$. (—) exact, (- - -) Lele's [1], (– – –) Lee and Seo's [11], (–·–) Kim and Lee's [13], and (—) the present scheme.

Overall it may be concluded from Figs. 3–5 that the present boundary schemes provide significantly improved resolution characteristics over the previous ones, especially compared with Lele's [1] and Lee and Seo's [11], which are based on second-order accuracy and small grid stencils. Providing the resolution limits that are listed in Table 4, the present boundary schemes show much lower levels of both dispersive and dissipative errors. It should be particularly noted that the present boundary schemes reach even higher resolution limits and stricter error tolerances. In terms of resolution limits and profiles it is proved that the present optimisation procedure works effectively for the boundary compact schemes. Prior to their application in an actual computation the numerical stability should be also validated, and this is done next.

4.3. Eigenvalue analysis

In order to confirm the numerical stability of the present boundary schemes in association with the interior scheme an eigenvalue analysis is performed. The analysis begins by considering a one-dimensional linear scalar wave equation:

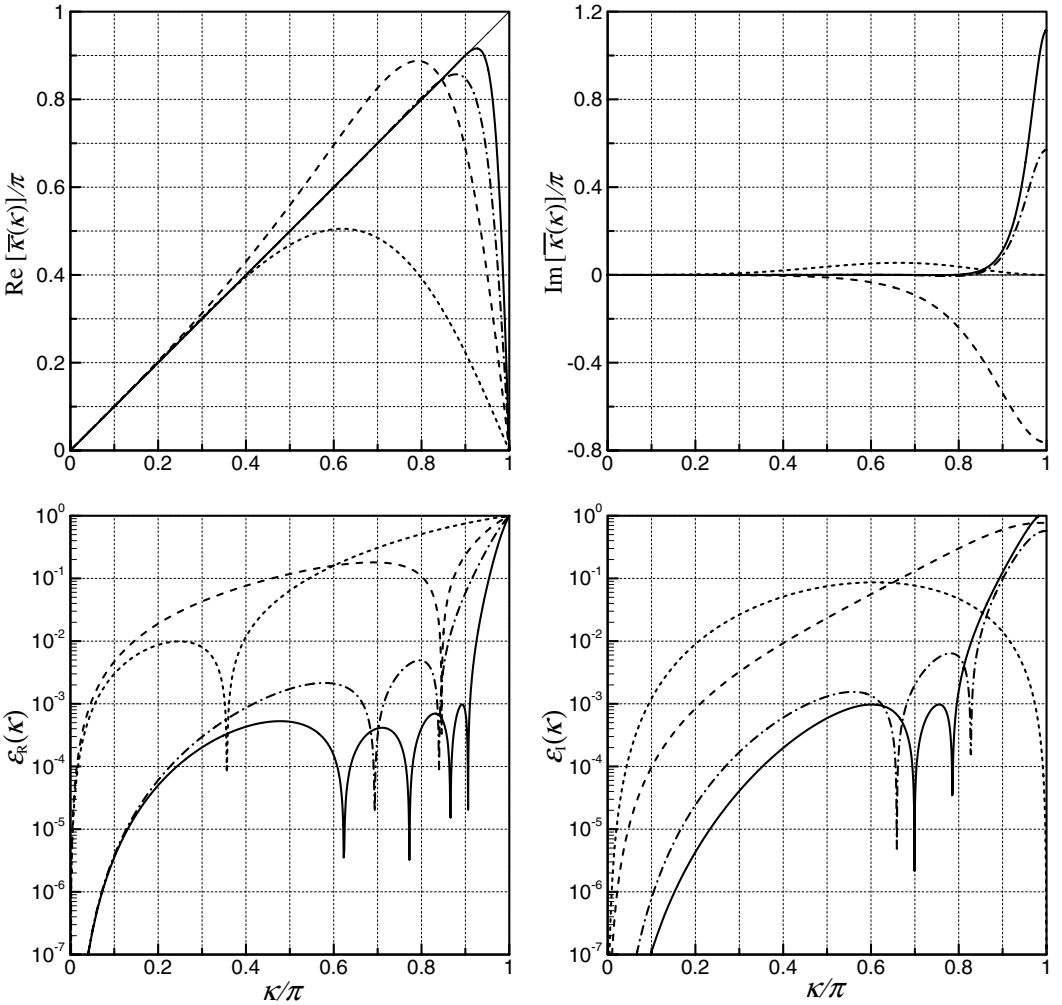

Fig. 5. Pseudo-wavenumber and resolution error diagrams of boundary compact schemes for $i = 2$. (—) exact, (- - -) Lele's [1], (– – –) Lee and Seo's [11], (–·–) Kim and Lee's [13], and (—) the present scheme.

$$\frac{\partial f}{\partial t} + c_\infty \frac{\partial f}{\partial x} = 0 \tag{36}$$

over a domain $x \in [0, L]$ with a prescribed boundary condition $f(x = 0, t) = f_b(t)$, where c_∞ is the wave convection speed. For the purpose of a stability analysis $f_b(t)$ can be set to zero without loss of generality [14]. The domain is discretised into N equal intervals ($N + 1$ nodes) with $\Delta x = L/N$. Imposing the boundary condition at the node $i = 0$ then leads to N unknowns to be found ($i = 1, \ldots, N$). The derivative $\partial f/\partial x$ in Eq. (36) is numerically evaluated by the finite difference schemes, which yields a linear system of equations expressed in a matrix–vector form as

$$\mathbf{P}\bar{\mathbf{f}}' = \frac{1}{\Delta x}\mathbf{Q}\mathbf{f}, \tag{37}$$

where $\mathbf{f}$ is an N-dimensional vector representing the values of the objective function at the nodes and $\bar{\mathbf{f}}'$ is a vector of the numerical derivatives:

$$\mathbf{f} = (f_1, f_2, \ldots, f_{N-1}, f_N)^{\mathrm{T}}, \quad \bar{\mathbf{f}}' = \left(\bar{f}'_1, \bar{f}'_2, \ldots, \bar{f}'_{N-1}, \bar{f}'_N\right)^{\mathrm{T}}. \tag{38}$$

In Eq. (37) $\mathbf{P}$ and $\mathbf{Q}$ represent $N \times N$ matrices in which the top two rows have been rearranged to eliminate $\bar{f}'_0$, which is redundant due to the fixed boundary condition on f_0:

$$\mathbf{P} = \begin{pmatrix} 1 & \gamma_{12}^* & \gamma_{13}^* & 0 & \cdots & 0 & 0 & 0 & 0 \\ \gamma_{21}^* & 1 & \gamma_{23}^* & \gamma_{24}^* & 0 & \cdots & 0 & 0 & 0 \\ \beta & \alpha & 1 & \alpha & \beta & 0 & \cdots & 0 & 0 \\ 0 & \beta & \alpha & 1 & \alpha & \beta & 0 & \cdots & 0 \\ \vdots & \ddots & \ddots & \ddots & \ddots & \ddots & \ddots & \ddots & \vdots \\ 0 & \cdots & 0 & \beta & \alpha & 1 & \alpha & \beta & 0 \\ 0 & 0 & \cdots & 0 & \gamma_{24} & \gamma_{23} & 1 & \gamma_{21} & \gamma_{20} \\ 0 & 0 & 0 & \cdots & 0 & \gamma_{13} & \gamma_{12} & 1 & \gamma_{10} \\ 0 & 0 & 0 & 0 & \cdots & 0 & \gamma_{02} & \gamma_{01} & 1 \end{pmatrix}, \tag{39}$$

$$\mathbf{Q} = \begin{pmatrix} b_{11}^* & b_{12}^* & b_{13}^* & b_{14}^* & b_{15}^* & b_{16}^* & 0 & 0 & 0 & \cdots & 0 \\ b_{21}^* & b_{22}^* & b_{23}^* & b_{24}^* & b_{25}^* & b_{26}^* & 0 & 0 & 0 & \cdots & 0 \\ -a_2 & -a_1 & 0 & a_1 & a_2 & a_3 & 0 & 0 & 0 & \cdots & 0 \\ -a_3 & -a_2 & -a_1 & 0 & a_1 & a_2 & a_3 & 0 & 0 & \cdots & 0 \\ 0 & -a_3 & -a_2 & -a_1 & 0 & a_1 & a_2 & a_3 & 0 & \cdots & 0 \\ \vdots & \ddots & \ddots & \ddots & \ddots & \ddots & \ddots & \ddots & \ddots & \ddots & \vdots \\ 0 & \cdots & 0 & -a_3 & -a_2 & -a_1 & 0 & a_1 & a_2 & a_3 & 0 \\ 0 & \cdots & 0 & 0 & -a_3 & -a_2 & -a_1 & 0 & a_1 & a_2 & a_3 \\ 0 & \cdots & 0 & 0 & -b_{26} & -b_{25} & -b_{24} & -b_{23} & -b_{22} & -b_{21} & -b_{20} \\ 0 & \cdots & 0 & 0 & -b_{16} & -b_{15} & -b_{14} & -b_{13} & -b_{12} & -b_{11} & -b_{10} \\ 0 & \cdots & 0 & 0 & -b_{06} & -b_{05} & -b_{04} & -b_{03} & -b_{02} & -b_{01} & -b_{00} \end{pmatrix}, \tag{40}$$

where the coefficients rearranged for the boundary condition are given by

$$(\gamma_{12}^*, \gamma_{13}^*) = (\gamma_{12} - \gamma_{10}\gamma_{02}, \gamma_{13})/(1 - \gamma_{10}\gamma_{01}), \tag{41}$$

$$(\gamma_{21}^*, \gamma_{23}^*, \gamma_{24}^*) = (\gamma_{10}\gamma_{21} - \gamma_{20}, \gamma_{10}\gamma_{23} - \gamma_{20}\gamma_{13}, \gamma_{10}\gamma_{24})/(\gamma_{10} - \gamma_{20}\gamma_{12}), \tag{42}$$

$$b_{1m}^* = (b_{1m} - \gamma_{10}b_{0m})/(1 - \gamma_{10}\gamma_{01}) \quad \text{for } m = 1, \ldots, 6, \tag{43}$$

$$b_{2m}^* = (\gamma_{10}b_{2m} - \gamma_{20}b_{1m})/(\gamma_{10} - \gamma_{20}\gamma_{12}) \quad \text{for } m = 1, \ldots, 6, \tag{44}$$

$$b_{nn} = -\sum_{m=0,\neq n}^{6} b_{nm} \quad \text{for } n = 0, 1, 2. \tag{45}$$

The Eqs. (41) and (43) are retrieved by cancelling $\bar{f}'_0$ out from Eqs. (23) and (24). Likewise Eqs. (42) and (44) follow from Eqs. (24) and (25).

Applying the numerical differentiation described as above to Eq. (36) then leads to a matrix–vector form:

$$\mathbf{P}\frac{\mathrm{d}\mathbf{f}}{\mathrm{d}t} = -\frac{c_\infty}{\Delta x}\mathbf{Q}\mathbf{f}. \tag{46}$$

Since Eq. (46) is a system of ordinary differential equations in time with constant coefficients the solution consists of normal modes $\mathbf{f} = \hat{\mathbf{f}}\mathrm{e}^{wt}$ with a constant w representing the rates of decay or amplification of the modes. Imposing the normal modes into Eq. (46) leads to an eigenvalue problem:

$$\mathbf{Q}\hat{\mathbf{f}} = -\omega\mathbf{P}\hat{\mathbf{f}}, \tag{47}$$

where $\omega = w\Delta x/c_\infty$ is the dimensionless eigenvalue and $\hat{\mathbf{f}}$ becomes the corresponding eigenvector. The real parts of the eigenvalues are required to be equal to or less than zero to guarantee the numerical stability of the present boundary schemes, i.e. $|\mathrm{e}^{wt}| \leqslant 1$. The eigenvalues are obtained numerically by the Mathematica.

Fig. 6 illustrates distributions of the eigenvalues in a complex plane for different sizes of the matrices, i.e. the numbers of nodes given. It is shown that most of the eigenvalues are located in the left half of the complex plane. However some of them marginally cross the y-axis on the positive side. Fig. 7 plots the maximum real parts of the eigenvalues where it is shown that the orders of magnitudes are relatively small and converging to zero as the number of nodes increases. It turns out that those components are neutrally stable in practice and do not cause any instability in the actual computations that follow.

4.4. Stability and convergence test

The numerical stability of the present boundary schemes is further assessed by putting Eq. (36) into actual calculations through the discretisation by Eq. (46). The initial and boundary conditions for the calculations are

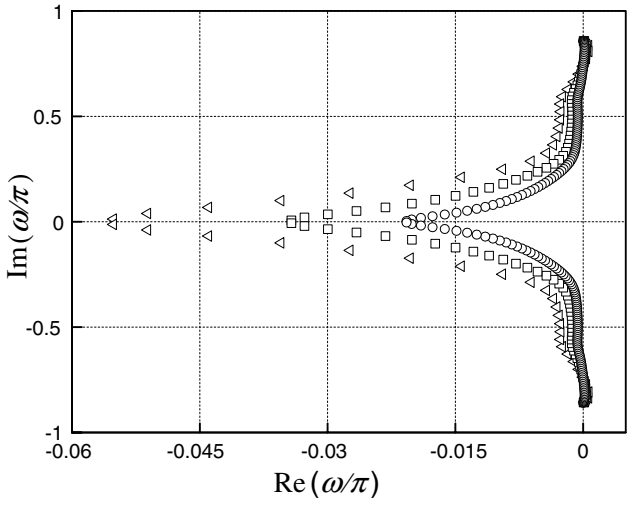

Fig. 6. Distribution of eigenvalues from Eq. (47). (◁) $N = 50$, (□) $N = 100$, and (○) $N = 200$.

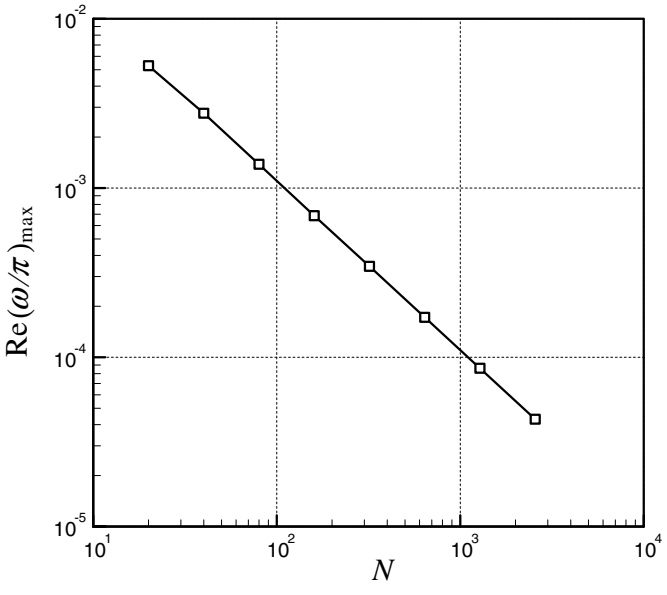

Fig. 7. Maximum real parts in the eigenvalues of Eq. (47) varying with number of nodes.

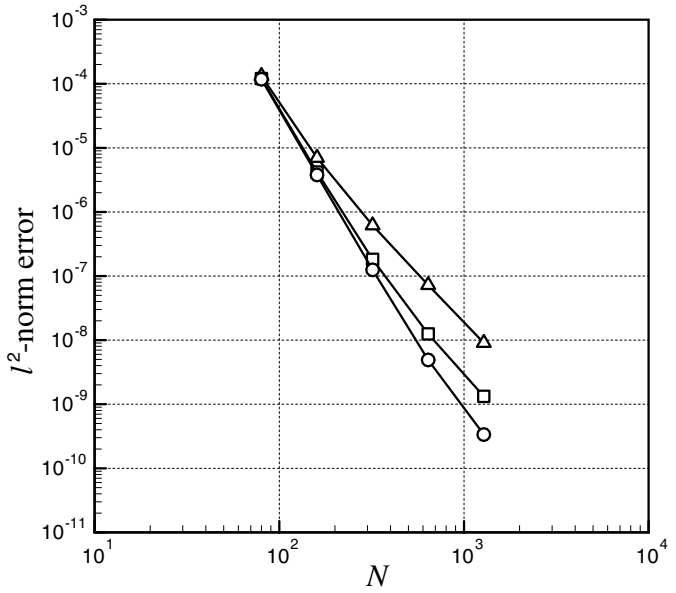

Fig. 8. Error levels measured at $c_\infty t/L = 100$ in calculation of Eq. (46) varying with number of nodes used. (—△) CFL = 1.0, (—□) CFL = 0.5, and (—○) CFL = 0.25.

$$f(x, t = 0) = f_\infty \sin(4\pi x/L), \quad 0 \leqslant x \leqslant L, \tag{48}$$

$$f(x = 0, t) = -f_\infty \sin(4\pi c_\infty t/L), \quad t \geqslant 0. \tag{49}$$

Then the exact solution to this initial boundary value problem is given by

$$f_{\text{exact}}(x, t) = f_\infty \sin[4\pi(x - c_\infty t)/L]. \tag{50}$$

Calculations are carried out on a range of uniform meshes with different grid spaces, i.e. number of nodes. The classical fourth-order Runge–Kutta scheme is used for integration of solutions in time. The time step sizes are determined by the CFL numbers specified. Three different CFL numbers are tested to investigate the influence of the time integration scheme. The calculations are carried out up to $t = 100L/c_\infty$. The errors of numerical solutions are measured at the final moment by the l^2-norm defined as $\sqrt{\sum_{i=1}^{N}(f_i - f_{\text{exact}})^2/(Nf_\infty^2)}$. The resulting error diagrams are plotted in Fig. 8 for various grid densities and CFL numbers. It is shown that the present boundary schemes consistently yield stable solutions and the solutions converge to the exact one as the number of nodes increases. It is also confirmed that the neutrally stable eigenvalue components do not harm the overall stability, independent of the time step.

5. Application to benchmark problems

In this section the performance of the present boundary schemes is demonstrated through their application to three different benchmark problems. These problems include one-dimensional scalar wave convection, two-dimensional vorticity wave convection and sound wave scattering in complex geometry. The accuracy of the numerical solutions is quantified by comparing with analytic solutions. The accuracy of the present boundary schemes is then compared with that of the previous ones in order to confirm the performance enhancement.

5.1. One-dimensional scalar wave convection

The one-dimensional scalar wave convection is chosen as the first benchmark problem. This problem simulates the convection of an initial wave pulse and its transmission through a computational boundary. Eq. (36)

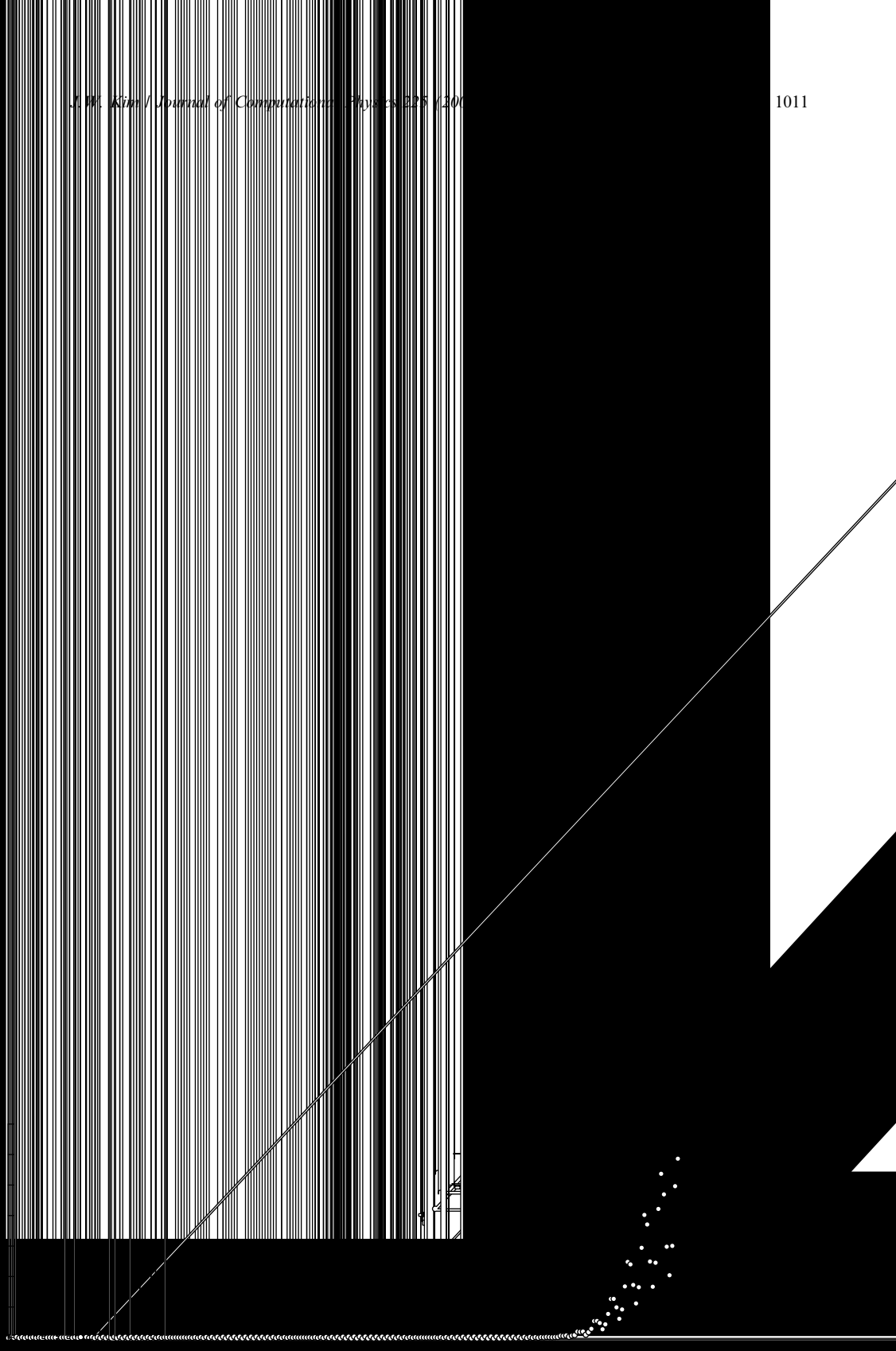

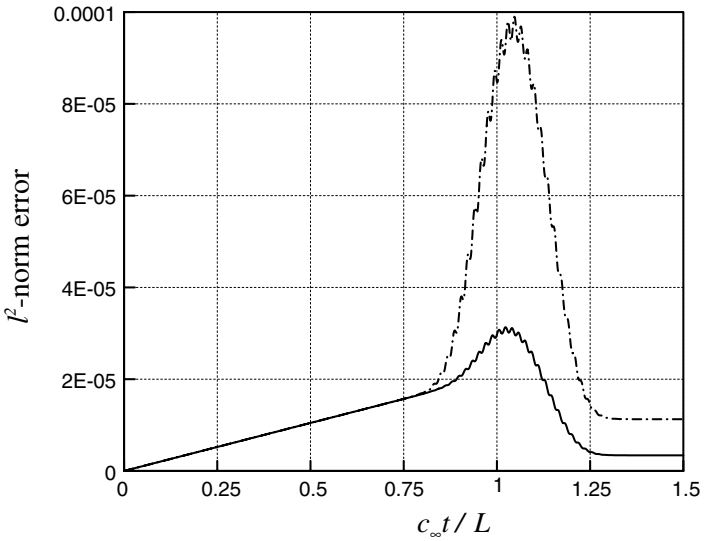

Fig. 10. Numerical error histories in calculation of one-dimensional scalar wave convection. (–·–) Kim and Lee's [13] and (—) the present boundary schemes. $N = 900$.

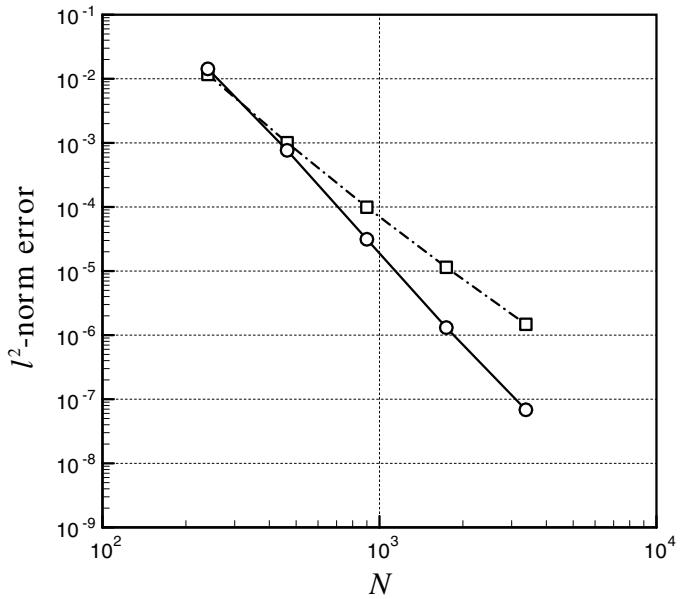

Fig. 11. Peak error levels in calculation of one-dimensional scalar wave convection varying with number of nodes used. (–·–□) Kim and Lee's [13] and (—○) the present boundary schemes.

with

$$\mathbf{Q} = \begin{pmatrix} \rho \\ \rho u \\ \rho v \\ \rho e_t \end{pmatrix}, \quad \mathbf{E} = \begin{pmatrix} \rho u \\ \rho u^2 + p \\ \rho v u \\ \rho(e_t + p)u \end{pmatrix} \quad \text{and} \quad \mathbf{F} = \begin{pmatrix} \rho v \\ \rho u v \\ \rho v^2 + p \\ \rho(e_t + p)v \end{pmatrix}, \tag{55}$$

where the total energy per unit mass is defined as $e_t = p/[(\gamma-1)\rho] + (u^2+v^2)/2$ and $\gamma = c_p/c_v$ is the ratio of specific heats. For air, $\gamma = 1.4$ in the present computation. The calculations are done over a domain $x \in [-0.5L, L]$ and $y \in [-0.75L, 0.75L]$ in which the initial isentropic vortex is given by

$$\left.\begin{aligned} \rho(x,y,t=0) &= \rho_\infty[1-(\gamma-1)\psi^2(x,y)/2]^{1/(\gamma-1)} \\ u(x,y,t=0) &= u_\infty + a_\infty(y/R)\psi(x,y) \\ v(x,y,t=0) &= -a_\infty(x/R)\psi(x,y) \\ p(x,y,t=0) &= p_\infty(\rho/\rho_\infty)^\gamma \end{aligned}\right\} \quad \text{for } -0.5L \leqslant x \leqslant L,\ -0.75L \leqslant y \leqslant 0.75L, \tag{56}$$

with

$$\psi(x,y) = \frac{\varepsilon}{2\pi}\sqrt{\exp[1-(x^2+y^2)/R^2]}, \tag{57}$$

where $R = 0.08L$ is given to specify the size of vortex and ε is a constant to determine the strength of vortex. $\varepsilon = 0.1$ is chosen for linear cases and higher values are tested for non-linear cases as well. The free stream velocity $u_\infty = M_\infty a_\infty$ is given by the Mach number $M_\infty = 2.0$, where $a_\infty = \sqrt{\gamma p_\infty/\rho_\infty}$ is the ambient speed of sound. This problem was previously used by Yee et al. [16] for their high-order shock-capturing methods and filters. The exact solution is simply given by

$$\left.\begin{aligned} \rho_{\text{exact}}(x,y,t) &= \rho_\infty[1-(\gamma-1)\psi^2(\hat{x},y)/2]^{1/(\gamma-1)} \\ u_{\text{exact}}(x,y,t) &= u_\infty + a_\infty(y/R)\psi(\hat{x},y) \\ v_{\text{exact}}(x,y,t) &= -a_\infty(\hat{x}/R)\psi(\hat{x},y) \\ p_{\text{exact}}(x,y,t) &= p_\infty(\rho/\rho_\infty)^\gamma \end{aligned}\right\} \quad \text{with } \hat{x} = x - u_\infty t. \tag{58}$$

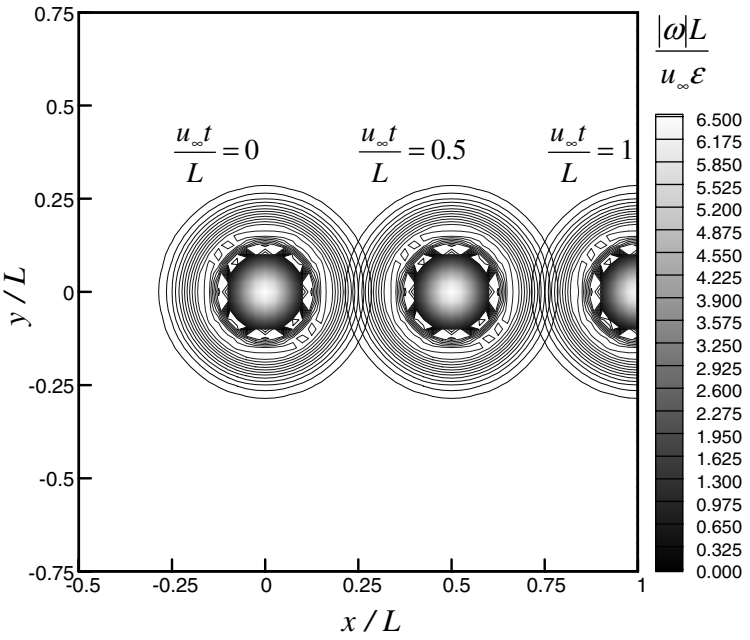

Fig. 12. Two-dimensional vorticity wave convection calculated by the present schemes. Contours of normalised absolute vorticity: $|\omega|L/(u_\infty\varepsilon)$. $\varepsilon = 0.1$. $(N \times N) = (60 \times 60)$.

Due to the supersonic free stream velocity the flow properties beyond the inlet boundary are invariant. Accordingly it is possible to let the x-direction flux derivatives in Eq. (54) be zero on $x < -0.5L$, which allows use of the interior scheme directly at the inlet boundary nodes ($i = 0, 1$ and 2) as in the previous case. On the other hand the boundary schemes are used at the exit boundary nodes ($i = N-2, N-1$ and N). The boundary schemes are also used at the lower ($j = 0, 1$ and 2) and upper boundary nodes ($j = N-2, N-1$ and N) in the y-direction. Numerical non-reflection boundary conditions [17] are implemented on the lower and upper boundaries to avoid spurious errors in the calculation. No boundary conditions are imposed at the exit boundary due to the supersonic outflow. The performance of the boundary schemes is examined while the wave packet passes through the exit boundary.

The classical fourth-order Runge–Kutta time integration is employed with CFL number 0.5. Fig. 12 shows time-traced contour plots of the two-dimensional wave convection calculated by the present schemes. Fig. 13 shows the wave profiles along the x-axis in comparison with the exact solution. A two-dimensional version of the l^2-norm error is defined as $\sqrt{\sum_{j=0}^{N}\sum_{i=0}^{N}(\omega_{i,j}-\omega_{\text{exact}})^2 L^2/[(N+1)\varepsilon u_\infty]^2}$ to measure the numerical error variation with time where $\omega = \partial v/\partial x - \partial u/\partial y$ is the vorticity. Fig. 14 shows the changes of numerical errors with

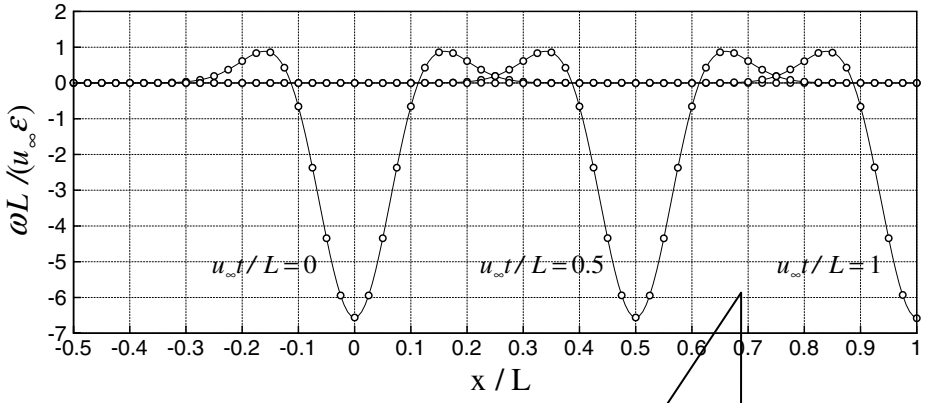

Fig. 13. Centreline profiles of two-dimensional vorticity wave along x-axis calculated by the present schemes. (—) exact and (○) numerical. $\varepsilon = 0.1$. $(N \times N) = (60 \times 60)$.

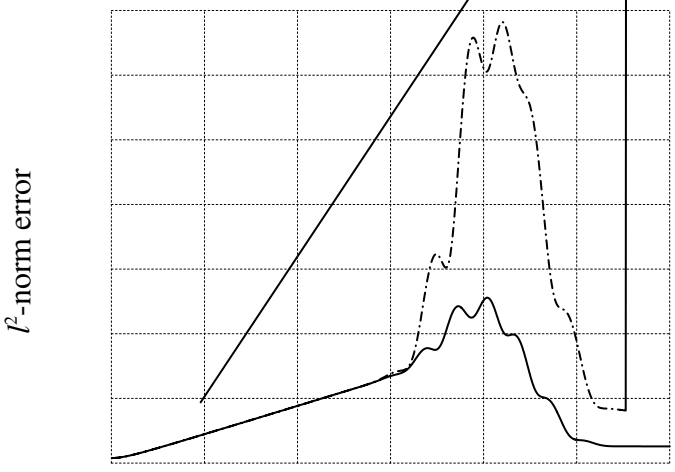

time. The peak error levels that occur in the vicinity of $t = L/u_\infty$ are plotted in Fig. 15 for the different numbers of nodes used. It is effectively demonstrated that the present boundary schemes generate more accurate solutions than the previous schemes do in two-dimensional applications also. In addition the same calculations are done in non-linear regime with higher values of ε as shown in Fig. 16, where $\varepsilon = 5$ is the fully non-linear

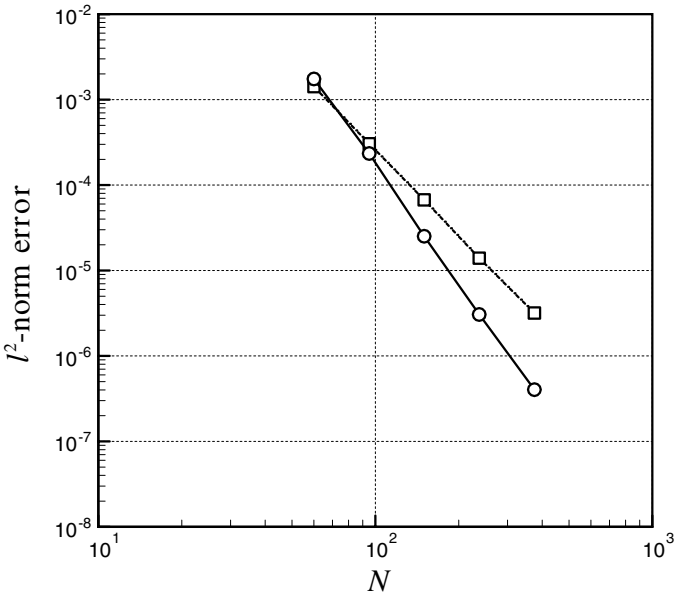

Fig. 15. Peak error levels in calculation of two-dimensional vorticity wave convection varying with number of nodes used. (–·–□) Kim and Lee's [13] and (—○) the present boundary schemes. $\varepsilon = 0.1$.

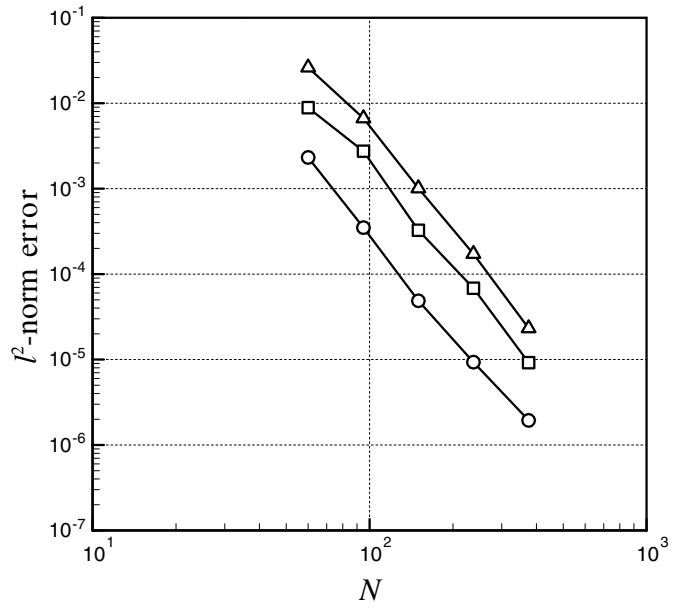

Fig. 16. Peak error levels in calculation of two-dimensional vorticity wave convection varying with number of nodes used. Non-linear calculation with the present schemes. (—△) $\varepsilon = 5$, (—□) $\varepsilon = 3$, and (—○) $\varepsilon = 1$.

case that was used in [16]. It is noticed that the proposed set of optimised compact schemes is capable of high-order accurate non-linear solutions without any filtering technique as long as the solution remains continuous.

5.3. Sound wave scattering in complex geometry

The last benchmark problem is two-dimensional sound wave scattering in complex geometry. This problem simulates a sound field scattered by two rigid circular cylinders of different sizes from a monopole acoustic source located between the cylinders in a zero mean flow. It was originally provided in the Fourth Computational Aeroacoustics Workshop on Benchmark Problems [18] and allows a stringent test on the performance of high-order CAA schemes when handling increasingly complex geometries. The calculation here involves the generalised two-dimensional compressible Euler equations in full conservation form with a source term as

$$\frac{\partial \widehat{\mathbf{Q}}}{\partial t}+\frac{\partial \widehat{\mathbf{E}}}{\partial \xi}+\frac{\partial \widehat{\mathbf{F}}}{\partial \eta}=\widehat{\mathbf{S}} \tag{59}$$

with

$$\widehat{\mathbf{Q}}=\mathbf{Q}/J,\quad \widehat{\mathbf{E}}=(\xi_x\mathbf{E}+\xi_y\mathbf{F})/J,\quad \widehat{\mathbf{F}}=(\eta_x\mathbf{E}+\eta_y\mathbf{F})/J \quad \text{and} \quad \widehat{\mathbf{S}}=(0,0,0,\dot{p}_s)^T/J. \tag{60}$$

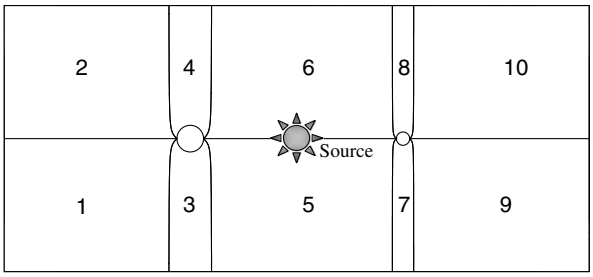

Fig. 17. Schematic diagram of computational domain decomposed into 10 virtual blocks for sound wave scattering in complex geometry.

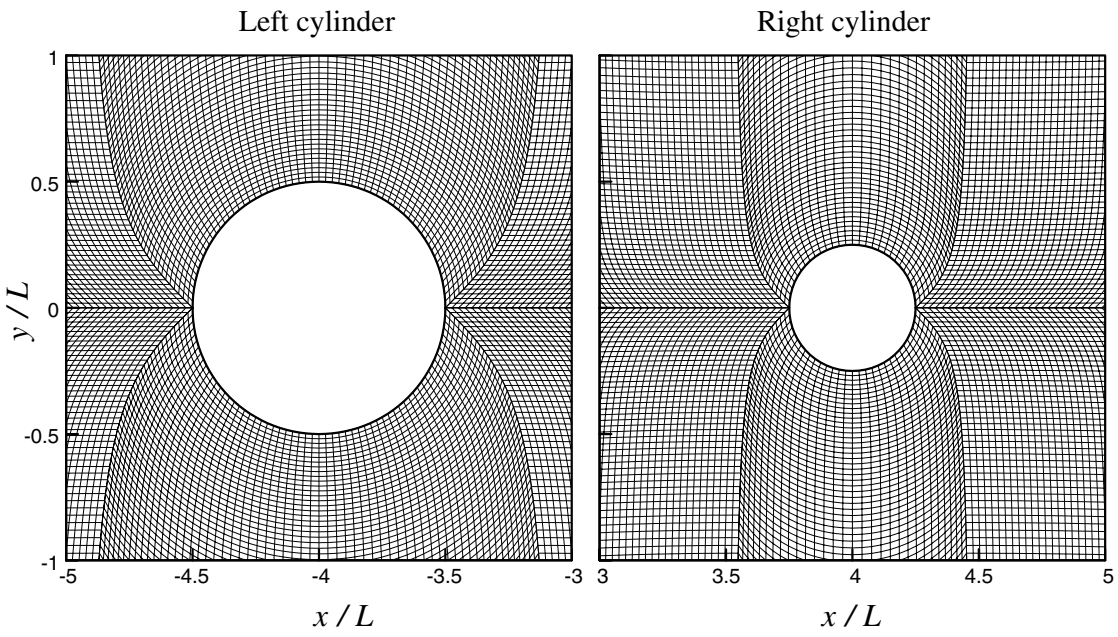

Fig. 18. H-topology grid mesh system for sound wave scattering in complex geometry.

The spatially distributed axisymmetric acoustic source is given by

$$\dot{p}_s = \varepsilon(\rho_\infty a_\infty^3/L)\sin(2\pi c_1 a_\infty t/L)\exp[-c_2(\ln 2)(x^2+y^2)/L^2], \tag{61}$$

where the constants are $\varepsilon = 0.1, c_1 = 4$ and $c_2 = 25$. The length scale L represents the diameter of the larger cylinder in this problem.

The computational domain is depicted in Fig. 17 and the H-topology grid mesh system is shown in Fig. 18. The entire domain is decomposed into 10 virtual blocks as illustrated in Fig. 17 along the singular lines where the grid metrics are discontinuous. In order to avoid the grid singularities each block is isolated in terms of numerical differentiation using the present boundary schemes, which do not cross the block boundaries. Interface conditions [19] are then implemented to restore correct physical communication between the isolated blocks. Non-reflecting boundary conditions [17] are used with a buffer layer [20] surrounding the physical domain. Wall boundary conditions [21] are imposed on the cylinder surfaces. The boundary schemes can be effectively tested in this problem due to the presence of many boundaries in a single domain.

The calculation is done over a domain $x \in [-9L, 9L]$ and $y \in [-4L, 4L]$ excluding the buffer layer. The bigger cylinder is located at $(-4L, 0)$ and the smaller one at $(4L, 0)$. The total number of nodes used is 166,400 (650×256) inside the domain. This provides 8 PPW (points per wavelength) on average, the highest 9.55 PPW is given on the cylinder surfaces and on block boundaries where some extra resolution is required. The classical fourth-order Runge–Kutta time integration is employed with CFL number 1. The calculation continues until $t = 40L/a_\infty$ and the collection of pressure data starts at $t = 30L/a_\infty$ when the transient waves due to the initial disturbances have completely disappeared.

The scattered sound pressure field calculated by the present schemes is plotted in Fig. 19. Interference between the radiating waves and the reflected waves is shown in the inner region. The scattered waves are clearly visualised in the outer region. The entire sound field is simulated well without any spurious noise due to the virtual boundaries and the walls. Fig. 20 presents the profiles of root-mean-squared (RMS) sound pressure plotted along the cylinder surfaces compared with analytic solution. The RMS sound pressure from the numerical solution is measured here by

$$p'_{\mathrm{RMS}} = \sqrt{\int_{t_1}^{t_2}(p-\bar{p})^2\,\mathrm{d}t/(t_2-t_1)} \quad \text{with } \bar{p} = \int_{t_1}^{t_2} p\,\mathrm{d}t/(t_2-t_1), \tag{62}$$

where $t_1 = 30L/a_\infty$ and $t_1 = 40L/a_\infty$. The analytic solution is derived from the linearised Euler equations and can be found in [18]. As shown in Fig. 20 the present solution agrees well with the analytic solution whereas the previous schemes yield noticeable errors. The superiority of the present boundary schemes is confirmed in a complex geometry application.

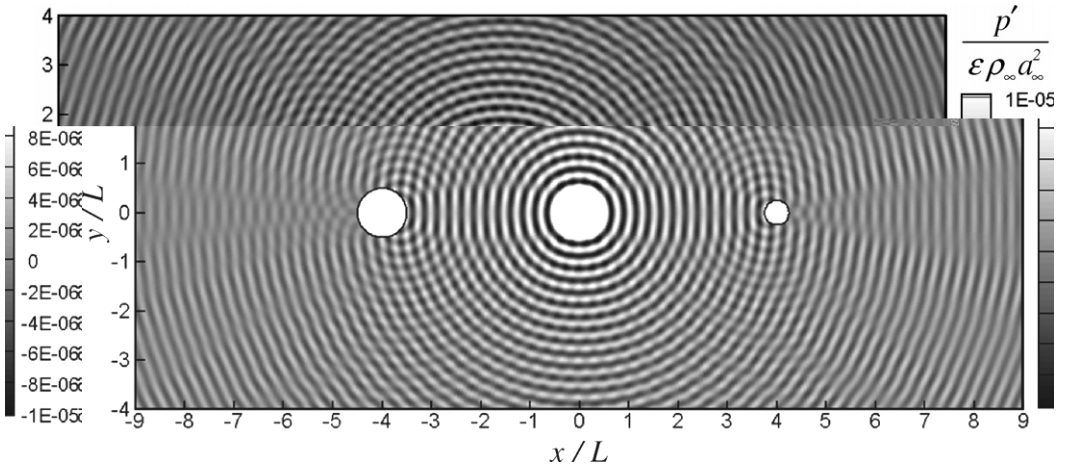

Fig. 19. Sound wave scattering in complex geometry calculated by the present schemes. Contours of normalised sound pressure at $t = 40\,L/a_\infty : p'/(\varepsilon\rho_\infty a_\infty^2)$.

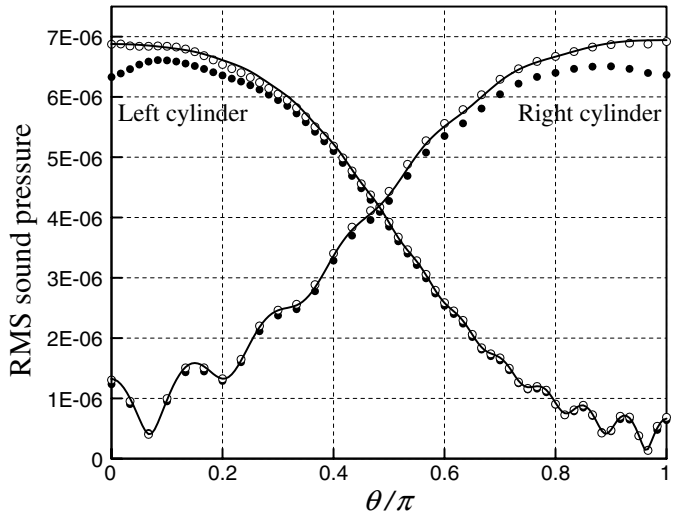

Fig. 20. Profiles of root-mean-squared sound pressure $p'_{\mathrm{RMS}}/(\varepsilon\rho_\infty a_\infty^2)$ along cylinder surfaces. (—) exact, (●) Kim and Lee's [13], and (○) the present boundary schemes.

6. Conclusions

A complete set of boundary compact finite difference schemes has been presented. The use of polynomial-trigonometric blended extrapolation functions has led to a new optimisation strategy achieving improved resolution characteristics of the boundary schemes. The eigenvalue analysis and numerical test have confirmed the overall stability of the new boundary schemes for the pentadiagonal matrix system. The proposed extrapolation functions should also be useful for optimisation of other types of compact schemes. The increased performance and accuracy of the new boundary schemes have been effectively demonstrated through their applications to single- and multi-dimensional benchmark problems. The new boundary schemes can be employed in a variety of practical CAA applications that use compact finite difference schemes, especially in complex geometries.

References

[1] S.K. Lele, Compact finite difference schemes with spectral-like resolution, J. Comput. Phys. 103 (1992) 16.
[2] M.A. Tolstykh, Application of fifth-order compact upwind differencing to moisture transport equation in atmosphere, J. Comput. Phys. 112 (1994) 394.
[3] J.A. Ekaterinaris, Implicit, high-resolution, compact schemes for gas dynamics and aeroacoustics, J. Comput. Phys. 156 (1999) 272.
[4] R. Hixon, Prefactored small-stencil compact schemes, J. Comput. Phys. 165 (2000) 522.
[5] J.B. Freund, S.K. Lele, P. Moin, Numerical simulation of a Mach 1.92 turbulent jet and its sound field, AIAA J. 38 (11) (2000) 2023.
[6] J.W. Kim, P.J. Morris, Computation of subsonic inviscid flow past a cone using high-order finite difference schemes, AIAA J. 40 (10) (2002) 1961.
[7] S. Nagarajan, S.K. Lele, J.H. Ferziger, A robust high-order compact method for large eddy simulation, J. Comput. Phys. 191 (2003) 392.
[8] J.W. Kim, D.J. Lee, Optimized compact finite difference schemes with maximum resolution, AIAA J. 34 (5) (1996) 887.
[9] N.A. Adams, K. Shariff, A high-resolution hybrid compact-ENO scheme for shock-turbulence interaction problems, J. Comput. Phys. 127 (1996) 27.
[10] D. Gaitonde, J.S. Shang, Optimized compact-difference-based finite-volume schemes for linear wave phenomena, J. Comput. Phys. 138 (1997) 617.
[11] C. Lee, Y. Seo, A new compact spectral scheme for turbulence simulations, J. Comput. Phys. 183 (2002) 438.
[12] G. Ashcroft, X. Zhang, Optimized prefactored compact schemes, J. Comput. Phys. 190 (2003) 459.
[13] J.W. Kim, D.J. Lee, Implementation of boundary conditions for optimized high-order compact scheme, J. Comput. Acoust. 5 (2) (1997) 177.
[14] M.H. Carpenter, D. Gottlieb, S. Abarbanel, The stability of numerical boundary treatments for compact high-order finite-difference schemes, J. Comput. Phys. 108 (1993) 272.

[15] C.K.W. Tam, Aliasing problem: category 1, problem 1, analytic solution, in: Proc. Fourth Computational Aeroacoustics Workshop on Benchmark Problems, Cleveland, USA, October 2003, NASA Glenn Research Centre (NASA/CP-2004-212954, 2004), p. 31.
[16] H.C. Yee, N.D. Sandham, M.J. Djomehri, Low-dissipative high-order shock-capturing methods using characteristic-based filters, J. Comput. Phys. 150 (1999) 199.
[17] J.W. Kim, D.J. Lee, Generalized characteristic boundary conditions for computational aeroacoustics, AIAA J. 38 (11) (2000) 2040.
[18] S.E. Sherer, Acoustic scattering from multiple circular cylinders: category 2, problems 1 and 2, analytic solution, in: Proc. Fourth Computational Aeroacoustics Workshop on Benchmark Problems, Cleveland, USA, October 2003, NASA Glenn Research Centre (NASA/CP-2004-212954, 2004), p. 39.
[19] J.W. Kim, D.J. Lee, Characteristic interface conditions for multiblock high-order computation on singular structured grid, AIAA J. 41 (12) (2003) 2341.
[20] R.D. Sandberg, N.D. Sandham, Nonreflecting zonal characteristic boundary condition for direct numerical simulation of aerodynamic sound, AIAA J. 44 (2) (2006) 402.
[21] J.W. Kim, D.J. Lee, Generalized characteristic boundary conditions for computational aeroacoustics, part 2, AIAA J. 42 (1) (2004) 47.